

Two-tooth bosonic quantum comb for temporal-correlation sensing

Shaojiang Zhu,* Xinyuan You, Alexander Romanenko, and Anna Grassellino

*Superconducting Quantum Materials and Systems Center,
Fermi National Accelerator Laboratory, Batavia, IL 60510, USA*

We introduce a two-tooth bosonic quantum comb that captures the sequential interactions between a thermal absorber and a long-lived coherent probe. The comb provides a causal, multi-time description of coherence transport, tracking how the probe records both instantaneous fluctuations and their temporal correlations. Using a process-tensor formulation, we derive closed-form expressions showing that interference between the two interaction windows generates a non-monotonic memory response that reflects a fundamental competition between the absorber's thermal population and its dynamical correlations. By sweeping the temporal separation between the interaction windows, the probe directly samples the absorber's population correlator, enabling bosonic noise spectroscopy that discriminates Markovian temperature noise from slow or spectrally structured fluctuations. The approach is readily compatible with circuit-QED platforms and offers a general method for probing fluctuating bosonic environments.

Thermal fluctuations constitute both a resource and a fundamental limitation across physics, governing decoherence in quantum devices, setting noise floors in precision sensors, and mediating energy flow in mesoscopic systems [1–9]. Accurately probing such fluctuations at the single-quantum level remains an outstanding challenge for quantum thermodynamics, condensed-matter physics, and superconducting circuits. At the quantum level, temperature manifests not as a static shift, but through the statistics and temporal correlations of energy-exchange events. Sensing strategies that access this dynamical structure are therefore essential for advancing quantum calorimetry and noise spectroscopy [10, 11].

A common approach is to infer temperature from the phase or coherence decay of a quantum probe coupled to a thermal mode [12, 13]. Single-interaction (one-tooth) schemes, including qubit-based thermometry, map instantaneous thermal fluctuations onto a dephasing envelope or phase shift [14–17]. While powerful, such approaches fundamentally treat the thermal bath as a memoryless noise source: each measurement interrogates only a single realization of the absorber's fluctuations, and is therefore blind to the temporal correlations that often dominate low-frequency thermodynamics in solid-state systems.

Here, we show that sequential interactions between a thermal mode and a coherent probe naturally form a bosonic quantum comb, a multi-time causal structure that captures how the probe acquires and transports information through memory [18–21]. In this picture, the probe stores the phase and noise imprint of a first interaction and interferes it with a second, enabling access to dynamical temperature signatures that are invisible to single-shot protocols. Using a Gaussian process-tensor framework, we derive a compact two-time memory kernel that yields analytic expressions for the probe visibil-

ity and the corresponding quantum Fisher information (QFI) [22, 23].

The resulting two-tooth comb displays a non-monotonic memory response: for short delays, preserved probe coherence allows the two interactions to interfere constructively, enhancing thermometric precision beyond any single-interaction scheme; for delays comparable to the absorber's correlation time, partially decayed correlations add dephasing without providing commensurate temperature information, thereby suppressing the QFI below the memoryless limit. This behavior reflects a fundamental competition between instantaneous thermal population and its temporal correlations, revealing when quantum memory amplifies or degrades coherence-based sensing.

By sweeping the delay between interactions, the probe directly samples the absorber's population correlator, enabling bosonic noise spectroscopy that distinguishes Markovian thermal noise from slow, correlated, or spectrally structured fluctuations [24, 25]. These results position multi-time bosonic probes as an experimentally accessible platform for probing fluctuating quantum environments and clarifying the role of memory in quantum sensing [26–28].

We consider a thermal absorber mode a , equilibrated with a local thermal bath, dispersively couples to a coherent probe mode b through a weak cross-Kerr interaction λ . The probe coherence is monitored by a readout transmon, which enables time-resolved interrogation of the two interaction windows defining the bosonic comb [Fig. 1(a)]. During each interaction window the effective Hamiltonian is $H_{\text{int}} = \lambda a^\dagger a b^\dagger b$, where λ is a cross-Kerr rate generated by a nonlinear coupler or qubit bridge. Thermal fluctuations of n_a induce both a deterministic phase shift and stochastic phase noise on the probe, encoding temperature information into the probe quadratures [29].

A key feature of the architecture is that the probe remains long-lived coherent [30, 31] and only weakly damped between interactions. The temperature-dependent phase imprinted during the first interaction

* szhu26@fnal.gov

is therefore preserved and coherently compared with the phase acquired in a second interaction. This sequence naturally forms a two-tooth bosonic quantum comb, as schematically illustrated in Fig. 1(b).

Physically, the two teeth sample the absorber's number fluctuations at distinct times, generating a coherence contribution proportional to the autocorrelation $\langle \delta n_a(t_1) \delta n_a(t_2) \rangle_T$. For delays much shorter than the characteristic correlation time $\Delta \ll \tau_c$, the two samples remain strongly correlated, so the probe effectively interferes two realizations of the same fluctuating field, leading to a memory-assisted enhancement of thermometric precision. As $\Delta \sim \tau_c$, the samples become only partially correlated and the same memory term primarily adds dephasing, producing a characteristic suppression of the QFI. The delay-dependent visibility of the two-tooth comb thus directly reflects the competition between the absorber's instantaneous thermal fluctuations and its dynamic correlations.

Operationally, the two-tooth protocol turns the probe into a coherent memory: the first interaction writes a temperature-dependent phase into the probe, free evolution carries that phase forward, and the second interaction interferes it with a later snapshot of the same thermal fluctuations [18].

Memory kernel: Within the Gaussian cross-Kerr model, the resulting two-tooth coherence takes the com-

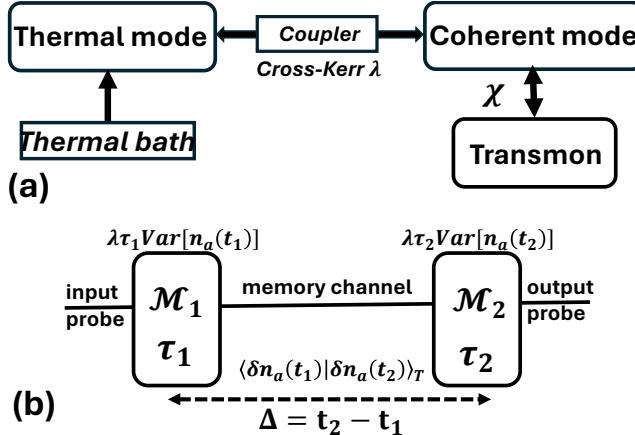


FIG. 1. **Schematic of two-tooth bosonic quantum comb for thermometry and noise discrimination.** (a) A thermal absorber mode a , equilibrated with a local thermal bath, couples dispersively to a long-lived coherent probe mode b via the cross-Kerr strength λ . Thermal fluctuations of n_a induce both a deterministic phase shift and stochastic phase noise on the probe, encoding temperature information into the probe quadratures. A transmon is used to monitor the probe coherence via the dispersive pull χ . (b) The sequence forms a two-tooth bosonic quantum comb: each tooth corresponds to an interaction map, while the probe's free evolution acts as a quantum memory channel linking them. The output probe state contains both (i) single-interaction phase diffusion $\lambda\tau_1 \text{Var}[n_a(t_1)]$ and (ii) mixed phase-phase terms proportional to the absorber's autocorrelation $\langle \delta n_a(t_1) \delta n_a(t_2) \rangle_T$.

pact form in the weak-dephasing regime [32].

$$C_2(\Delta, T) = C_1^{(1)}(\tau_1, T) C_1^{(2)}(\tau_2, T) \exp[-2\lambda^2 \tau_1 \tau_2 \mathcal{K}(\Delta, T)]. \quad (1)$$

with the single-interaction coherence for tooth j

$$C_1^{(j)}(\tau_j, T) = e^{-(\lambda\tau_j)^2 \bar{n}_a(T)}, \quad j \in \{1, 2\}, \quad (2)$$

and the absorber's population autocorrelation function

$$\mathcal{K}(\Delta, T) = \langle \delta n_a(t_1) \delta n_a(t_2) \rangle_T. \quad (3)$$

The absorber follows a fluctuating population trajectory $n_a(t) = \bar{n}_a + \delta n_a(t)$, and the two interaction windows simply sample this trajectory at times t_1 and $t_2 = t_1 + \Delta$.

Eq. (1) makes the memory physics explicit. The product $C_1^{(1)}(\tau_1, T) C_1^{(2)}(\tau_2, T)$ is the benchmark obtained by probing two independent noise realizations, while the exponential “kernel factor” encodes how strongly the two interactions are correlated in time. For slow absorber dynamics $\mathcal{K}(\Delta, T) \approx \mathcal{K}(0, T)$ and $\Delta \ll \tau_c$, both teeth interrogate nearly the same fluctuation history and the correlated dephasing exceeds the naive product of single-tooth visibilities. For intermediate delays $\Delta \sim \tau_c$, the kernel has decayed but remains finite, so the same memory term predominantly adds dephasing without providing a commensurate coherent imprint, and the two-tooth visibility can drop below the independent benchmark. In the Markovian limit, $\mathcal{K}(\Delta, T) \rightarrow 0$ and $C_2(\Delta, T) \rightarrow C_1^{(1)}(\tau_1, T) C_1^{(2)}(\tau_2, T)$ shows that the two-tooth comb smoothly reduces to a memoryless Ramsey-like sequence[see Fig. 2(f)].

The behavior of the memory kernel underlying the two-tooth protocol is summarized in Fig. 2(a)-(c). Here, we assume an exponentially decaying kernel form

$$\mathcal{K}(\Delta; T) = \bar{n}_a \tilde{\mathcal{K}}(\Delta, T), \quad \tilde{\mathcal{K}} = e^{-\Delta/\tau_c(T)}, \quad (4)$$

which corresponds to a Lorentzian absorber noise spectrum with correlation time $\tau_c(T)$ [33, 34]. Panel (a) shows how the Lorentzian correlation kernel in Eq. (4) evolves with T and Δ , highlighting the exponential decay of thermal photon-number correlations at each temperature: usable thermal memory decays more rapidly as the absorber is warmed. The white dashed curve marks the contour where $\tilde{\mathcal{K}} = \bar{n}_a e^{-1}$, indicating that the correlation amplitude has dropped to $1/e$ of its zero-delay value. Panel (b) displays the pure amplitude gain factor $(1 + \tilde{\mathcal{K}})$ appearing in Eq. (D5), which quantifies the correlation-induced boost to the phase variance. This correlated gain is broad and substantial at low temperature but narrows rapidly as the absorber's correlation time decreases with increasing T . Panel (c) shows the relative kernel responsivity $\partial_T \tilde{\mathcal{K}} / (1 + \tilde{\mathcal{K}})$, which governs how memory effects modify the temperature slope of the QFI. Following the $1/e$ dashed contour approximately, where $\partial_T \tilde{\mathcal{K}}$ is largest in magnitude, the responsivity develops a pronounced negative ridge, reflecting strong competition with the population responsivity. We will show that this competition can locally suppress the memory efficiency and generate regions where $\mathcal{A} < 1$.

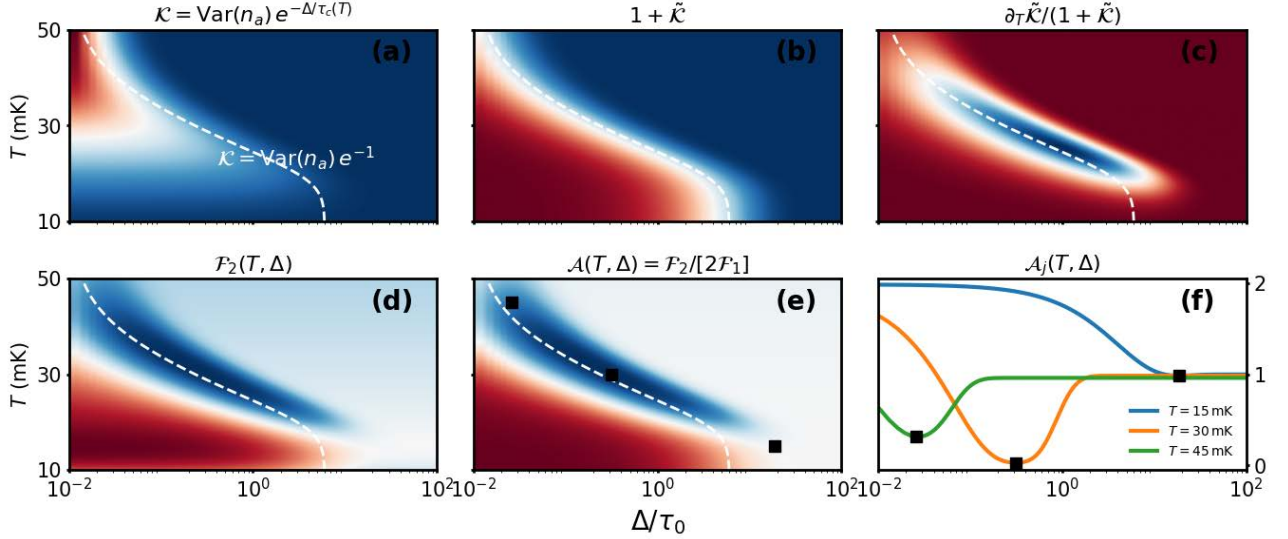


FIG. 2. **Memory kernel and non-monotonic memory response of the two-tooth comb** [32]. (a) Lorentzian correlation kernel (Eq. (4)) showing the exponential correlation envelope and its temperature-dependent decay. The white dashed curve denotes $\tilde{\mathcal{K}} = e^{-1}$ (i.e., $\Delta = \tau_c(T)$). (b) Pure amplitude gain factor $1 + \partial_T \tilde{\mathcal{K}}$, which quantifies the correlation-induced boost to the probe's phase variance. (c) Relative responsivity $\partial_T \tilde{\mathcal{K}}/(1 + \tilde{\mathcal{K}})$, revealing the locus of minimum temperature sensitivity and a strong competition with the population responsivity (d) Two-tooth quantum Fisher information \mathcal{F}_2 , inheriting the non-monotonic behavior of the kernel's responsivity and correlation decay. (e) Corresponding memory advantage $\mathcal{A} = \mathcal{F}_2/[2\mathcal{F}_1]$, showing enhancement ($\mathcal{A} > 1$) at short delays where correlations dominate and suppression ($\mathcal{A} < 1$) where temperature responsivities compete. Black markers indicate the delay at which \mathcal{A} reaches its minimum for selected temperatures. (f) Line cuts of $\mathcal{A}(\Delta)$ at three representative temperatures (15, 30, and 45 mK). At low temperature, the minimum of \mathcal{A} is shifted away from the $1/e$ contour due to the weak temperature dependence of the correlation time, whereas at higher temperatures the minimum aligns with the correlation-time boundary.

memory efficiency: Using the one- and two-tooth coherence envelopes Eq. (2) and (1), we obtain the corresponding one-tooth QFI [32]

$$\mathcal{F}_1^{(j)}(\tau_j) = \frac{2\partial_T^2 C_1^{(j)}}{1 - C_1^{(j)}} = \frac{[\lambda\tau_j \bar{n}_a \partial_T \bar{n}_a C_1^{(j)}]^2}{1 - C_1^{(j)}}, \quad (5)$$

and two-tooth QFI

$$\mathcal{F}_2(\Delta) = \frac{2\partial_T^2 \Gamma_{\phi_2} C_2^2}{1 - C_2^2}, \quad (6)$$

$$\partial_T \Gamma_{\phi_2} = \frac{1}{2} \lambda^2 (\tau_1^2 + \tau_2^2) \partial_T \bar{n}_a + \lambda^2 \tau_1 \tau_2 \partial_T \mathcal{K}(\Delta),$$

with $\partial_T \bar{n}_a \approx \hbar\omega_a \bar{n}_a / k_B T^2$ with $\bar{n}_a \ll 1$.

Thus, temporal correlations open an additional channel for the two-tooth temperature information, carried by the derivative of the memory kernel rather than by instantaneous number fluctuations alone. To quantify this effect, we define the memory efficiency

$$\mathcal{A}(\Delta) = \frac{\mathcal{F}_2(\Delta)}{\mathcal{F}_1^{(1)}(\tau_1) + \mathcal{F}_1^{(2)}(\tau_2)}, \quad (7)$$

which, in the weak-dephasing regime, tends to $\mathcal{A} \rightarrow 1$ whenever $\mathcal{K} \rightarrow 0$.

Using the same kernel model in Eq. (4) and taking the two identical teeth ($\tau_1 = \tau_2$), we evaluate the two-tooth

\mathcal{F}_2 and the corresponding $\mathcal{A} = \mathcal{F}_2/2\mathcal{F}_1$. The results are summarized in Fig. 2(d)–(f). Notably, both \mathcal{F}_2 and \mathcal{A} exhibit a characteristic non-monotonic behavior, showing either enhancement or suppression depending on the absorber temperature and the separation between the two teeth. We suggest that this behavior arises from a competition between the absorber's thermal population and its temporal correlations.

To make this competition explicit, we rewrite Eq. (7) in the weak-dephasing limit [32]

$$\mathcal{A} = (1 + \tilde{\mathcal{K}}) \left[1 + \frac{\partial_T \tilde{\mathcal{K}}/(1 + \tilde{\mathcal{K}})}{\partial_T \bar{n}_a / \bar{n}_a} \right]^2, \quad (8)$$

with the Lorentzian memory kernel expressed in Eq. (4). The prefactor $(1 + \tilde{\mathcal{K}}) \geq 1$ acts as a gain knob that quantifies how correlated fluctuations increase the total phase variance. The bracketed factor encodes the competition between two temperature responsivities: the population responsivity $S_{\bar{n}_a} = \partial_T \bar{n}_a / \bar{n}_a$ and the correlation responsivity $S_{\tilde{\mathcal{K}}} = \partial_T \tilde{\mathcal{K}}/(1 + \tilde{\mathcal{K}})$. When $S_{\tilde{\mathcal{K}}}$ reinforces $S_{\bar{n}_a}$, memory sharpens the temperature slope and enhances \mathcal{F}_2 ($\mathcal{A} > 1$). When $S_{\tilde{\mathcal{K}}}$ partially cancels $S_{\bar{n}_a}$, the net slope is reduced and correlations can degrade \mathcal{F}_2 , driving \mathcal{A} below unity ($\mathcal{A} < 1$).

We emphasize that the structure of Eq. (4) is generic: for any correlated noise source whose dephasing can be

decomposed into a diagonal (population) term and a two-time kernel, the relative size and sign of the two responsiveness $S_{\bar{n}_a}$ and $S_{\bar{\mathcal{K}}}$ in Eq. (8) determine whether correlations enhance or suppress metrological performance.

Correlated Noise Spectra The memory kernel \mathcal{K} in Eq. (3) also represents the absorber's population autocorrelation function if we sweep the delay Δ between the two tooth of the comb, thereby changing the probe coherence $C_2(\Delta)$ in Eq. (1) [35]. As a result, the two-tooth protocol provides a direct means of mapping the absorber's noise spectrum.

This noise correlator is related to the spectral density of number fluctuations by the Wiener-Khinchin relation [36],

$$\mathcal{K}(\Delta) = \int_{-\infty}^{\infty} \frac{d\omega}{2\pi} S_{nn}(\omega) e^{-i\omega\Delta}, \quad (9)$$

so that the observable two-tooth coherence $C_2(\Delta)$ inherits its delay dependence from the underlying spectrum $S_{nn}(\omega)$ via Eq. (1). Varying Δ thus implements a bosonic noise-spectroscopy protocol in which a single long-lived probe mode interrogates both the equal-time variance and the temporal correlations of the absorber population. Equivalently, in the standard filter-function

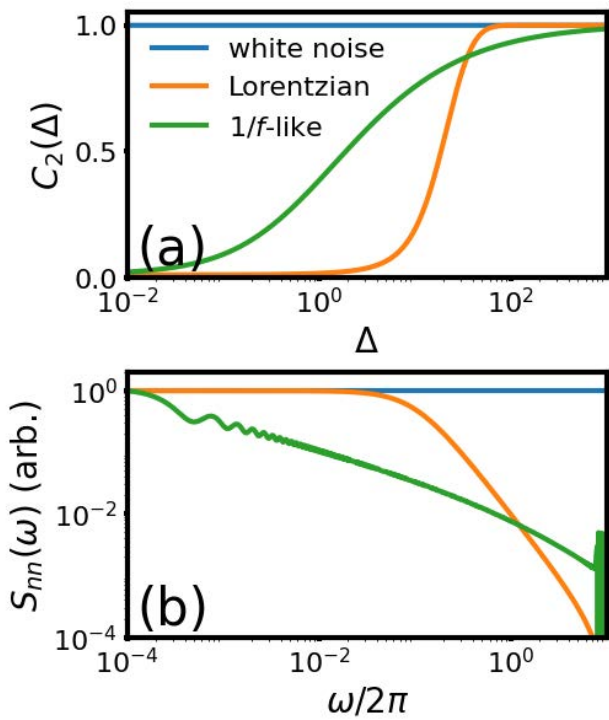


FIG. 3. **Delay-dependent visibility for different absorber noise spectra** [32]. (a) Normalized two-tooth coherence $\tilde{C}_2(\Delta)$ for white, Lorentzian, and $1/f$ -like population noise, showing flat, sharp, and broad delay-dependent rolloffs, respectively. (b) Corresponding normalized spectra $\tilde{S}_{nn}(\omega)$ reconstructed from $\tilde{C}_2(\Delta)$, yielding flat, finite-bandwidth, and low-frequency-dominated line shapes.

language, the two-tooth sequence defines a comb-like frequency response that imposes an oscillatory weighting $\sim \cos(\omega\Delta)$ on $S_{nn}(\omega)$, so that varying Δ moves these fringes across frequency and reshapes the noise seen by the probe [1].

As a result, distinct noise environments produce qualitatively different delay dependence of $C_2(\Delta)$. The two-tooth comb therefore provides a minimally invasive, fully passive method for diagnosing correlated or non-Markovian thermal dynamics using only weak cross-Kerr coupling and a long-lived bosonic probe. Because $\mathcal{K}(\Delta)$ and $S_{nn}(\omega)$ are Fourier duals, the measured visibility curve $C_2(\Delta)$ can be viewed as a processed but still direct fingerprint of the population-fluctuation spectrum.

Figure 3 illustrates how the two-tooth comb discriminates distinct noise environments. Panel (a) shows the normalized delay-dependent coherence $\tilde{C}_2(\Delta)$: white noise yields a flat response, Lorentzian noise exhibits a sharp crossover near the correlation time, and $1/f$ -like noise produces a broad, slowly varying rolloff. Panel (b) shows the corresponding spectra $\tilde{S}_{nn}(\omega)$ reconstructed from $\tilde{C}_2(\Delta)$, giving flat (white), finite-bandwidth (Lorentzian), and slowly decaying, low-frequency-dominated ($1/f$ -like) spectra. This one-to-one mapping demonstrates that scanning Δ allows the two-tooth comb to function as a bosonic noise spectrometer, distinguishing Markovian white noise, finite-time correlations, and slow, heavy-tailed fluctuations.

From an applications perspective, this makes the two-tooth comb a natural diagnostic tool for correlated noise in cryogenic detectors and quantum sensors. In high-energy and nuclear physics settings, where calorimeters, resonator-based photon detectors, and qubit-enabled sensors are increasingly limited by slow fluctuators, quasiparticle bursts, and radiation-induced noise, the same bosonic mode used for sensing can be repurposed as a temporal noise spectrometer [37–39]. More broadly, the protocol can be applied to structured environments in superconducting circuits, optomechanical devices, and spin-ensemble platforms, providing a minimally invasive way to fingerprint non-Markovian thermal dynamics *in situ*.

In addition, by repeating the two-tooth measurement at different temperatures, one can track how the extracted noise parameters (e.g., variance and correlation time) evolve with T , providing temperature-resolved diagnostics such as slow two-level fluctuators or quasiparticles [40, 41]. But we leave this as a natural extension of the present work.

Experimental Outlook Superconducting circuits provide a natural platform for realizing the two-tooth bosonic comb. A high-quality 3D cavity with milliseconds lifetime acts as the long-lived probe [30, 31, 42], while a lower-frequency resonator or terminated transmission line functions as the thermal absorber. A weak cross-Kerr interaction generated by a fixed-frequency transmon or static nonlinear coupler imprints the absorber's fluctuations onto the probe during each inter-

action window [17, 43–45]. Interaction timing can be set by short cavity-drive pulses or virtual displacements, and the final probe coherence is read out via standard dispersive qubit measurement. No fast flux control or active modulation is required, and all elements operate in the regime already demonstrated in circuit-QED experiments. These considerations indicate that the two-tooth comb can be implemented with existing hardware and measured using standard microwave techniques.

Summary We introduced a two-tooth bosonic quantum comb that elevates quantum thermometry from single-interaction phase detection to a genuinely multi-time interference protocol. In this architecture, a long-lived probe mode acts as a coherent memory: it stores the temperature-dependent phase from the first interaction and interferes it with a second interaction to access temporal correlations of the thermal absorber. This coherent recycling generates a correlation term in the probe coherence that yields a memory-assisted enhancement of the QFI at short delays, enabling higher sensitivity and broader operating flexibility than any single-tooth scheme and making the protocol attractive for practical thermometry and calorimetry.

Meanwhile, the formalism reveals a complementary regime in which memory becomes a *disadvantage*: when the delay exceeds the absorber correlation time or the

probe coherence time, residual correlations are washed out and the second interaction contributes primarily extra dephasing, driving the two-tooth sensitivity below the single-tooth benchmark. Therefore, this regime provides a controlled setting to investigate how environmental memory impacts metrological performance, offering a quantitative probe of dynamical noise processes and fundamental precision limits.

Looking ahead, multi-tooth generalizations promote the protocol to a genuine multi-time noise spectrometer for bosonic environments, enabling reconstruction of population correlators, spectral densities, and energy-exchange pathways in mesoscopic baths. The framework is broadly applicable across cavity QED, optomechanics, and magnonics, and offers a route to memory-assisted sensing, noise characterization, and control in realistic circuit-QED platforms using only standard dispersive couplings and long-lived cavity modes.

acknowledgments. This work was supported by the U.S. Department of Energy, Office of Science, National Quantum Information Science Research Centers, Superconducting Quantum Materials and Systems Center (SQMS), under Contract No. 89243024CSC000002. Fermilab is managed by FermiForward Discovery Group, LCC, acting under Contract No. 89243024CSC000002.

[1] A. A. Clerk, M. H. Devoret, S. M. Girvin, F. Marquardt, and R. J. Schoelkopf, Introduction to quantum noise, measurement, and amplification, *Rev. Mod. Phys.* **82**, 1155 (2010).

[2] S. Kudzialek, P. Dulian, J. Majsak, S. Chakraborty, and R. Demkowicz-Dobrzański, Quantum metrology using quantum combs and tensor network formalism, *New J. Phys.* **27**, 013019 (2025).

[3] S. Barzanjeh, M. Aquilina, and A. Xuereb, Manipulating the flow of thermal noise in quantum devices, *Phys. Rev. Lett.* **120**, 060601 (2018).

[4] S. Campbell, I. d’Amico, M. A. Ciampini, *et al.*, Roadmap on quantum thermodynamics, *Quantum Sci. Technol.* (2025).

[5] J. Bylander, S. Gustavsson, F. Yan, F. Yoshihara, *et al.*, Noise spectroscopy through dynamical decoupling with a superconducting flux qubit, *Nat. Phys.* **7**, 565 (2011).

[6] M. G. Paris, Quantum estimation for quantum technology, *Int. J. Quantum Inf.* **7**, 125 (2009).

[7] T. M. Stace, Quantum limits of thermometry, *Phys. Rev. A* **82**, 011611 (2010).

[8] F. Mallet, M. Castellanos-Beltran, H. Ku, S. Glancy, E. Knill, *et al.*, Quantum state tomography of an itinerant squeezed microwave field, *Phys. Rev. Lett.* **106**, 220502 (2011).

[9] P. Krantz, M. Kjaergaard, F. Yan, T. P. Orlando, S. Gustavsson, and W. D. Oliver, A quantum engineer’s guide to superconducting qubits, *Appl. Phys. Rev.* **6** (2019).

[10] B. Karimi, F. Brange, P. Samuelsson, and J. P. Pekola, Reaching the ultimate energy resolution of a quantum detector, *Nat. Commun.* **11**, 367 (2020).

[11] E. Gümüş, D. Majidi, D. Nikolić, *et al.*, Calorimetry of a phase slip in a josephson junction, *Nat. Phys.* **19**, 196 (2023).

[12] A. De Pasquale and T. M. Stace, Quantum thermometry, in *Thermodynamics in the Quantum Regime: Fundamental Aspects and New Directions* (Springer, 2019) pp. 503–527.

[13] A. Sharafiev, M. Juan, M. Cattaneo, and G. Kirchmair, Leveraging collective effects for thermometry in waveguide quantum electrodynamics, *Phys. Rev. Lett.* **134**, 213602 (2025).

[14] D. S. Lvov, S. A. Lemziakov, E. Ankerhold, J. T. Peltonen, and J. P. Pekola, Thermometry based on a superconducting qubit, *Phys. Rev. Appl.* **23**, 054079 (2025).

[15] J. Medford, J. Beil, J. Taylor, *et al.*, Self-consistent measurement and state tomography of an exchange-only spin qubit, *Nat. Nanotechnol.* **8**, 654 (2013).

[16] A. Sultanov, M. Kuzmanović, A. V. Lebedev, and G. S. Paraoanu, Protocol for temperature sensing using a three-level transmon circuit, *Appl. Phys. Lett.* **119** (2021).

[17] S. Zhu, X. You, A. Romanenko, and A. Grassellino, Coherence-mediated quantum thermometry in a hybrid circuit-QED architecture, *arXiv:2510.16318* (2025).

[18] G. Chiribella, G. M. D’Ariano, and P. Perinotti, Memory effects in quantum channel discrimination, *Phys. Rev. Lett.* **101**, 180501 (2008).

[19] M. Wang, D. J. Perez-Morelo, G. Ramer, *et al.*, Beating thermal noise in a dynamic signal measurement by a nanofabricated cavity optomechanical sensor, *Sci. Adv.* **9**, eadf7595 (2023).

[20] J. Roslund, R. M. De Araujo, S. Jiang, C. Fabre, and N. Treps, Wavelength-multiplexed quantum networks with ultrafast frequency combs, *Nat. Photon.* **8**, 109 (2014).

[21] M. Chen, N. C. Menicucci, and O. Pfister, Experimental realization of multipartite entanglement of 60 modes of a quantum optical frequency comb, *Phys. Rev. Lett.* **112**, 120505 (2014).

[22] W. Zhong, Z. Sun, J. Ma, X. Wang, and F. Nori, Fisher information under decoherence in bloch representation, *Phys. Rev. A* **87**, 022337 (2013).

[23] J. Liu, H. Yuan, X.-M. Lu, and X. Wang, Quantum Fisher information matrix and multiparameter estimation, *J. Phys. A: Math. Theor.* **53**, 023001 (2020).

[24] A. Das and R. Demkowicz-Dobrzański, Quantum metrology in presence of correlated noise via markovian embedding, [arXiv:2509.19685](https://arxiv.org/abs/2509.19685) (2025).

[25] E. Dumitrescu and T. S. Humble, Discrimination of correlated and entangling quantum channels with selective process tomography, *Phys. Rev. A* **94**, 042107 (2016).

[26] A. Altherr and Y. Yang, Quantum metrology for non-markovian processes, *Phys. Rev. Lett.* **127**, 060501 (2021).

[27] T. Van Der Lught, J. Barrett, and G. Chiribella, Device-independent certification of indefinite causal order in the quantum switch, *Nat. Commun.* **14**, 5811 (2023).

[28] F. Bussières, C. Clausen, A. Tiranov, B. Korzh, V. B. Verma, S. W. Nam, F. Marsili, A. Ferrier, P. Goldner, H. Herrmann, *et al.*, Quantum teleportation from a telecom-wavelength photon to a solid-state quantum memory, *Nat. Photon.* **8**, 775 (2014).

[29] A. Blais, A. L. Grimsmo, S. M. Girvin, and A. Wallraff, Circuit quantum electrodynamics, *Rev. Mod. Phys.* **93**, 025005 (2021).

[30] A. Romanenko, R. Pilipenko, S. Zorzetti, D. Frolov, *et al.*, Three-dimensional superconducting resonators at $T < 20$ mK with photon lifetimes up to $\tau = 2$ s, *Phys. Rev. Appl.* **13**, 034032 (2020).

[31] M. Reagor, H. Paik, G. Catelani, L. Sun, *et al.*, Reaching 10 ms single photon lifetimes for superconducting Aluminum cavities, *Appl. Phys. Lett.* **102** (2013).

[32] See Supplemental Material for derivations of the coherence transport, noise discrimination, and data analysis.

[33] D. Mickelsen, H. M. Carruzzo, S. N. Coppersmith, and C. C. Yu, Effects of temperature fluctuations on charge noise in quantum dot qubits, *Phys. Rev. B* **108**, 075303 (2023).

[34] P. J. de Visser, J. Baselmans, J. Bueno, N. Llombart, and T. Klapwijk, Fluctuations in the electron system of a superconductor exposed to a photon flux, *Nat. Commun.* **5**, 3130 (2014).

[35] G. A. Álvarez and D. Suter, Measuring the spectrum of colored noise by dynamical decoupling, *Phys. Rev. Lett.* **107**, 230501 (2011).

[36] P. J. Brockwell and R. A. Davis, *Introduction to time series and forecasting* (Springer, 2002).

[37] B. A. Mazin, Microwave kinetic inductance detectors: The first decade, in *AIP Conf. Proc.*, Vol. 1185 (American Institute of Physics, 2009) pp. 135–142.

[38] A. P. Vepsäläinen, A. H. Karamlou, J. L. Orrell, A. S. Dogra, *et al.*, Impact of ionizing radiation on superconducting qubit coherence, *Nature* **584**, 551 (2020).

[39] F. Sefkow, A. White, K. Kawagoe, R. Pöschl, and J. Repond, Experimental tests of particle flow calorimetry, *Rev. Mod. Phys.* **88**, 015003 (2016).

[40] C. Quintana, Y. Chen, D. Sank, *et al.*, Observation of classical-quantum crossover of 1/f flux noise and its paramagnetic temperature dependence, *Phys. Rev. Lett.* **118**, 057702 (2017).

[41] M. Lucas, A. Danilov, L. Levitin, A. Jayaraman, A. Casey, *et al.*, Quantum bath suppression in a superconducting circuit by immersion cooling, *Nat. Commun.* **14**, 3522 (2023).

[42] T. Kim, T. Roy, X. You, A. C. Li, H. Lamm, O. Pronitchev, *et al.*, Ultracoherent superconducting cavity-based multiqudit platform with error-resilient control, [arXiv:2506.03286](https://arxiv.org/abs/2506.03286) (2025).

[43] M. Bal, A. A. Murthy, S. Zhu, *et al.*, Systematic improvements in transmon qubit coherence enabled by Niobium surface encapsulation, *npj Quantum Inf.* **10**, 43 (2024).

[44] M. Kounalakis, C. Dickel, A. Bruno, N. Langford, and G. Steele, Tuneable hopping and nonlinear cross-kerr interactions in a high-coherence superconducting circuit, *npj Quantum Inf.* **4**, 38 (2018).

[45] N. Didier, J. Bourassa, and A. Blais, Fast quantum non-demolition readout by parametric modulation of longitudinal qubit-oscillator interaction, *Phys. Rev. Lett.* **115**, 203601 (2015)

Appendix A: Coherence Envelope

Because the accumulated phase noise results from many small, independent fluctuations and can be approximated by Gaussian diffusion (central limit theorem), the coherence state after dephasing can be described as a phase-averaged mixture

$$\rho_b(T) = \int d\phi P(\phi) |\alpha e^{i\phi}\rangle\langle\alpha e^{i\phi}|,$$

with Gaussian distribution $P(\phi) = \frac{e^{-\phi^2/2\sigma_\phi^2}}{\sqrt{2\pi\sigma_\phi^2}}$. The coherence envelope is the overlap of the initial coherent state with the diffused mixture:

$$C(\tau, T) = \langle\alpha|\rho_b(T)|\alpha\rangle = \int d\phi P(\phi) |\langle\alpha|\alpha e^{i\phi}\rangle|^2,$$

and can be evaluated exactly:

$$C(\tau, T) = \exp \left[-2|\alpha|^2 (1 - e^{-\sigma_\phi^2/2}) \right]. \quad (\text{A1})$$

with $\sigma_\phi^2 = \text{Var}(\phi_b)$ being the coherent phase variance. For the simplicity, we set the photon number in the probe $|\alpha|^2 = 1$ in the following discussions.

One-tooth coherence envelope. We consider a coherent probe mode initially prepared in $|\alpha\rangle$, coupled dispersively to a thermal absorber mode a through the cross-Kerr interaction $H_{\text{int}} = \lambda \hat{n}_a \hat{n}_b$, where λ is the cross-Kerr rate. During an interaction of duration τ , the probe accumulates a phase conditioned on the instantaneous thermal photon number,

$$|\alpha\rangle \rightarrow |\alpha e^{i\phi_b}\rangle, \quad \phi_b = \lambda n_a \tau.$$

Fluctuations of n_a in a thermal state therefore induce random probe phases.

For a thermal mode with mean occupation $\bar{n}_a(T) = [\exp(\hbar\omega_a/k_B T) - 1]^{-1}$, the number fluctuations is $\text{Var}(n_a) = \bar{n}_a(1 + \bar{n}_a)$. In the limit $\bar{n}_a \ll 1$ at low temperatures, $\text{Var}(n_a) \approx \bar{n}_a$ and we keep this approximation in the work.

The induced phase therefore has variance

$$\sigma_\phi^2 = \text{Var}(\phi_b) = (\lambda\tau)^2 \bar{n}_a. \quad (\text{A2})$$

Substituting Eq. (A2) in Eq. (A1) gives the one-tooth coherence envelope:

$$C_1(\tau) = \exp \left[-2(1 - e^{-\Gamma_\phi}) \right], \quad (\text{A3})$$

with the effective dephasing rate $\Gamma_\phi = \frac{1}{2}(\lambda\tau)^2 \bar{n}_a$. In the weak dephasing regime $\Gamma_\phi \ll 1$, Eq. (A3) is simplified as

$$C_1(\tau) = \exp \left[-(\lambda\tau)^2 \bar{n}_a \right], \quad (\text{A4})$$

and its first-order approximation is $C_1 \approx 1 - (\lambda\tau)^2 \bar{n}_a$.

Two-tooth coherence envelope. We now extend the one-tooth analysis to the case of two-tooth interactions. The coherent probe b interacts dispersively with the thermal absorber a during two windows of durations τ_1 and τ_2 , centered at times t_1 and $t_2 = t_1 + \Delta$, respectively. During each window, the dynamics are governed by the same cross-Kerr Hamiltonian: $H_{\text{int}} = \lambda \hat{n}_a \hat{n}_b$.

For a fixed trajectory of the absorber occupation, the probe acquires a phase

$$\phi_2 = \lambda [\tau_1 n_a(t_1) + \tau_2 n_a(t_2)],$$

so that an initial coherent state $|\alpha\rangle$ is mapped to $|\alpha e^{i\phi_2}\rangle$ after both interactions. The absorber fluctuations render ϕ_2 a random variable. We focus on the phase fluctuations relative to a temperature-independent mean, so that $\langle\phi_2\rangle$ is removed by demodulation and only the variance enters the coherence envelope.

We assume that the absorber number fluctuations are stationary and that the relevant statistics are well captured by their second moments. Therefore, the population autocorrelation function at delay Δ and fixed temperature T can be expressed as:

$$\mathcal{K}(\Delta) = \langle \delta n_a(t_1) \delta n_a(t_2) \rangle, \quad (\text{A5})$$

with $\delta n_a(t) = n_a(t) - \bar{n}_a$. The two-tooth phase variance $\text{Var}(\phi_2)$ reads

$$\sigma_{\phi_2}^2 = \lambda^2 \left[(\tau_1^2 + \tau_2^2) \text{Var}(n_a) + 2\tau_1\tau_2 \mathcal{K}(\Delta) \right]. \quad (\text{A6})$$

with $\text{Var}(n_a) = \bar{n}_a$, and $\mathcal{K}(\Delta)$ encodes the temporal correlations of the population fluctuations.

Substituting Eq. (A6) into Eq. (A1) yields the two-tooth coherence envelope

$$C_2(\Delta) = \exp \left\{ -2 \left[1 - e^{-\frac{1}{2}\lambda^2 [(\tau_1^2 + \tau_2^2)\bar{n}_a + 2\tau_1\tau_2 \mathcal{K}]} \right] \right\}, \quad (\text{A7})$$

with the effective two-tooth dephasing rate $\Gamma_{\phi_2} = \frac{1}{2}\lambda^2 [(\tau_1^2 + \tau_2^2)\bar{n}_a + 2\tau_1\tau_2 \mathcal{K}]$. In the weak dephasing regime, we can again simplify Eq. (A7) and get Eq. (1) discussed in the maintext.

$$\begin{aligned} C_2(\Delta) &= \exp \left\{ -\lambda^2 [(\tau_1^2 + \tau_2^2)\bar{n}_a - 2\tau_1\tau_2 \mathcal{K}] \right\} \\ &= C_1^{(1)}(\tau_1) C_1^{(2)}(\tau_2) \exp(-2\lambda^2 \tau_1 \tau_2 \mathcal{K}), \end{aligned} \quad (\text{A8})$$

It is clearly seen that, for slow absorber dynamics, $\mathcal{K} \approx \bar{n}_a$ represents the coherence enhancement due to the two-tooth correlation; for fast dynamics $\mathcal{K} \rightarrow 0$, C_2 reduces to the product of two uncorrelated interactions.

The first-order approximation of Eq. (A8) is $C_2(\Delta) \approx 1 - \lambda^2 [(\tau_1^2 + \tau_2^2)\bar{n}_a + 2\tau_1\tau_2 \mathcal{K}]$.

Appendix B: Quantum Fisher Information (QFI)

We consider a qubit probe initialized in the superposition $|+\rangle = (|0\rangle + |1\rangle)/\sqrt{2}$. Temperature-dependent fluctuations in the coupled environment induce pure dephasing during an interaction of duration τ , producing the

reduced density matrix

$$\rho = \frac{1}{2} \begin{pmatrix} 1 & C \\ C & 1 \end{pmatrix},$$

where C is the temperature-dependent coherence envelope (Ramsey visibility). The interaction produces temperature-independent phase shift; the deterministic phase accumulated in our dispersive setting is temperature independent and removed by standard demodulation.

The corresponding Bloch vector is

$$\vec{r} = (C, 0, 0), \quad r = |\vec{r}| = C.$$

For any qubit state undergoing pure dephasing, the QFI for estimating T reduces to a single “radial” term [22, 23]:

$$\mathcal{F}_T = \frac{(\partial_T C)^2}{1 - C^2}. \quad (\text{B1})$$

This expression reflects the fact that all temperature information is encoded solely in the decay of coherence; there is no phase-sensitive contribution because the eigenvectors of $\rho(T)$ are temperature independent.

The same expression applies directly to the bosonic probe used in the two-tooth comb approach. After one or two interaction windows, the probe’s reduced state is characterized by a complex visibility whose phase is temperature independent; thus only its magnitude C carries temperature information.

One-tooth QFI. Differentiating Eq. (A4) and substituting into Eq. (B1), we get the one-tooth coherence QFI

$$\mathcal{F}_1(\tau) = \frac{(\partial_T \Gamma_{\phi_1} e^{-\Gamma_{\phi_1}})^2 C_1^2}{1 - C_1^2}, \quad (\text{B2})$$

with $\partial_T \Gamma_{\phi_1} = (\lambda \tau)^2 \bar{n}_a \partial_T \bar{n}_a$. This expression characterizes the fundamental temperature sensitivity of a single coherence-mediated sampling of the absorber.

Two-tooth QFI. Differentiating the two-tooth coherence envelope Eq. (A8) and substituting into Eq. (B1), we have the full expression of the two-tooth QFI

$$\mathcal{F}_2(\Delta) = \frac{\left[2e^{-\Gamma_{\phi_2}} \partial_T \Gamma_{\phi_2}\right]^2 C_2^2}{1 - C_2^2}, \quad (\text{B3})$$

with $\partial_T \Gamma_2 = \frac{1}{2} \lambda^2 (\tau_1^2 + \tau_2^2) \partial_T n_a + \lambda^2 \tau_1 \tau_2 \partial_T \mathcal{K}$.

We define the memory efficiency as

$$\mathcal{A}(T, \Delta) = \frac{\mathcal{F}_2}{\mathcal{F}_1^{(1)} + \mathcal{F}_1^{(2)}}, \quad (\text{B4})$$

or equivalently as a difference

$$\mathcal{F}_{\text{mem}} = \mathcal{F}_2 - (\mathcal{F}_1^{(1)} + \mathcal{F}_1^{(2)}).$$

This framework captures how population correlations enhance the effective temperature sensitivity of the probe.

Appendix C: Correlated Noise Spectra

The absorber’s temporal correlations are fully encoded in $\mathcal{K}(\Delta)$, which is related to the noise spectrum via the Wiener-Khinchin theorem:

$$\mathcal{K}(\Delta) = \frac{1}{2\pi} \int_{-\infty}^{\infty} S_{nn}(\omega) e^{-i\omega\Delta} d\omega.$$

Thus, measuring $C_2(\Delta)$ is equivalent to accessing $\mathcal{K}(\Delta)$ and therefore $S_{nn}(\omega)$. Here, we assume the probe mode remains infinitely coherent and the only source of dephasing is the absorber mode associated with memory kernel $\mathcal{K}_a(\Delta)$. Isolating the correlated contribution gives

$$\ln C_2(\Delta) + \lambda^2(\tau_1^2 + \tau_2^2) \text{Var}(n_a) = -2\lambda^2 \tau_1 \tau_2 \mathcal{K}(\Delta).$$

The autocorrelation function can therefore be reconstructed as

$$\mathcal{K}(\Delta) = -\frac{1}{2\lambda^2 \tau_1 \tau_2} \left[\ln C_2(\Delta) + \lambda^2(\tau_1^2 + \tau_2^2) \text{Var}(n_a) \right]. \quad (\text{C1})$$

Fourier transforming Eq. (C1) yields the reconstructed spectrum:

$$S_{nn}(\omega) = 2 \int_0^{\infty} \mathcal{K}(\Delta) \cos(\omega\Delta) d\Delta. \quad (\text{C2})$$

Appendix D: Kernel Model and Memeroy Efficiency

In Fig. 2, we illustrate how a temperature-dependent absorber memory kernel shapes both the two-tooth QFI and the associated memory efficiency. Here we summarize the kernel model, the explicit expressions used to compute the plotted quantities, and the physical content of each panel.

We consider a thermal absorber with photon-number fluctuations characterized by a Lorentzian autocorrelation,

$$\mathcal{K}(\Delta; T) = \bar{n}_a(T) e^{-\Delta/\tau_c(T)}, \quad (\text{D1})$$

where Δ is the time separation between the two interaction windows, $\bar{n}_a(T)$ is the thermal photon number, and $\tau_c(T)$ is a temperature-dependent correlation time. For concreteness we take a smooth crossover between a long correlation time τ_{max} at low temperature and a short correlation time τ_{min} at high temperature,

$$\tau_c(T) = \frac{\tau_{\text{max}} + \tau_{\text{min}} r(T)}{1 + r(T)}, \quad r(T) = \left(\frac{T}{T_c}\right)^{\gamma},$$

where T_c sets the crossover temperature and γ controls the sharpness of the transition.

In Fig. 2 we fix $\tau_{\text{max}} = 6\tau_0$, $\tau_{\text{min}} = 0.01\tau_0$, $T_c = 20$ mK, and $\gamma = 8$, and scan temperatures 10 mK $\leq T \leq 50$ mK and delays $10^{-2}\tau_0 \leq \Delta \leq 10^2\tau_0$ on a logarithmic grid, with τ_0 being a reference time used only to render the delay axis dimensionless.

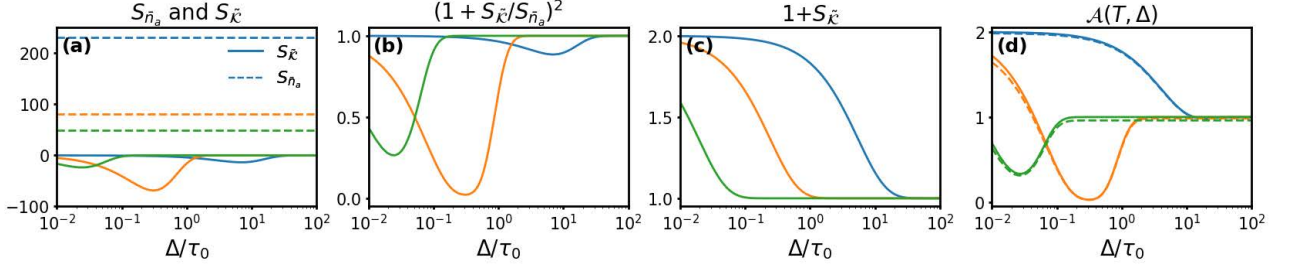


FIG. 4. **Competition between population and correlation responsivities in the two-tooth memory advantage.** (a) Linecuts of the absorber population responsivity $S_{\bar{n}_a}$ (dashed) and the correlation responsivity $S_{\bar{K}}$ (solid) as a function of delay Δ for selected temperatures: 15 mK (Blue), 30 mK (yellow), and 45 mK (green). (b) Responsivity factor $(1 + S_{\bar{K}}/S_{\bar{n}_a})^2$ entering the approximate expression for the memory efficiency. (c) Amplitude gain $1 + \bar{K}$, illustrating the decay of temporal correlations with increasing delay. (d) Approximate memory advantage $\mathcal{A} \simeq (1 + \bar{K})(1 + S_{\bar{K}}/S_{\bar{n}_a})^2$ for the same temperatures, showing regions of enhancement ($\mathcal{A} > 1$) and suppression ($\mathcal{A} < 1$) arising from the competition between thermal population responsivity and kernel responsivity. Dashed-lines are reproduced from Fig. 2(f).

To isolate the temporal structure of the correlations, we work with the normalized kernel

$$\tilde{K}(T, \Delta) = \frac{K(\Delta; T)}{K(0; T)} = e^{-\Delta/\tau_c(T)},$$

and characterize the temperature sensitivity of the memory kernel itself with the defined kernel responsivity

$$\tilde{S}(T, \Delta) = \left| \partial_T \tilde{K}(T, \Delta) \right| = \tilde{K}(T, \Delta) \frac{\Delta}{\tau_c(T)^2} |\partial_T \tau_c(T)|.$$

This definition describes how fast the kernel dephases with the temperature.

The absorber is modeled as a single bosonic mode of frequency $\omega_a/2\pi = 1$ GHz with mean thermal occupation \bar{n}_a . We can rewrite, respectfully, the one- and two-tooth coherence envelopes Eq. (A4) and (A8) as

$$C_j = e^{-\Gamma_{\phi_j}}, \quad j \in \{1, 2\}, \quad (\text{D2})$$

with $\Gamma_{\phi_1}(T) = g\bar{n}_a(T)$ and $\Gamma_{\phi_2}(\Delta, T) = g\bar{n}_a(T)[1 + 2\tilde{K}(\Delta, T)]$. We choose $g = 0.05$ to maintain the probe in the weak dephasing regime.

The corresponding QFI can be generally expressed as

$$\mathcal{F}_j = \frac{\partial_T^2 C_j}{1 - C_j^2} = \frac{\partial_T^2 \Gamma_{\phi_j}}{e^{2\Gamma_{\phi_j}} - 1}, \quad j \in \{1, 2\}, \quad (\text{D3})$$

and the memory efficiency with two identical teeth is

$$\mathcal{A} = \frac{\mathcal{F}_2}{2\mathcal{F}_1}. \quad (\text{D4})$$

Fig. 2(a) shows how the Lorentzian correlation kernel in Eq. (D1) evolves with T and Δ , highlighting the exponential decay of thermal photon-number correlations at each temperature: usable thermal memory decays more rapidly as the absorber is warmed. The white dashed curve marks the contour where $\tilde{K} = \text{Var}(n_a)e^{-1}$, indicating the correlation-time boundary at which the kernel amplitude has dropped to $1/e$ of its zero-delay value.

Fig. 2(b) displays the pure amplitude gain factor $(1 + \tilde{K})$ appearing in Eq. (D5), which quantifies the correlation-induced boost to the probe's phase variance. This correlated gain is broad and substantial at low temperature but narrows rapidly as the absorber's correlation time decreases with increasing T .

Fig. 2(c) shows the relative kernel responsivity $S_{\bar{K}} = \partial_T \tilde{K}/(1 + \tilde{K})$, which determines how memory modifies the temperature derivative of the QFI. Following the $1/e$ dashed contour—where $|\partial_T \tilde{K}|$ is maximized— \mathcal{S} forms a pronounced negative ridge, revealing a strong competition with the population responsivity that can suppress the memory efficiency.

Fig. 2(d) presents the resulting two-tooth QFI $\mathcal{F}_2(T, \Delta)$, which inherits the non-monotonic structure of the kernel's temperature responsivity: correlations enhance the QFI at short delays but eventually diminish as fluctuations decorrelate.

Fig. 2(e) shows the corresponding memory advantage $\mathcal{A}(T, \Delta) = \mathcal{F}_2/[2\mathcal{F}_1]$. Regions with $\mathcal{A} > 1$ reflect correlation-assisted enhancement, while regions with $\mathcal{A} < 1$ arise where the negative responsivity ridge in panel (c) overwhelms the positive population slope. Green markers indicate the delay at which \mathcal{A} reaches its minimum for selected temperatures.

Fig. 2(f) gives line cuts of $\mathcal{A}(\Delta)$ at three temperatures (15, 30, and 45 mK). At low temperature, the minimum of \mathcal{A} is shifted away from the $1/e$ contour because $\tau_c(T)$ is nearly temperature-independent, causing $\partial_T \tilde{K}$ to peak at a different delay. At higher temperatures, where $\tau_c(T)$ varies more strongly, the minimum aligns with the correlation-time boundary.

Physical insight. We suggest that the non-monotonic behavior of the two-tooth QFI observed in Fig. 2 arises from a competition between two physically distinct sources of probe dephasing: the absorber's mean thermal occupation and its temporal correlations.

We factorize the memory kernel Eq. (D1) as

$$\mathcal{K} = \bar{n}_a e^{-\Delta/\tau_c} = \bar{n}_a \tilde{\mathcal{K}},$$

where \bar{n}_a is the absorber's mean thermal occupation and $\tilde{\mathcal{K}}$ captures the normalized decay of population correlations through the correlation time $\tau_c(T)$.

Using the first-order approximation $1 - e^x \approx -x$, $x \ll 1$, Eq. (D3) can be rewritten as

$$\mathcal{F}_j = \partial_T^2 \Gamma_{\phi_j} / 2 \Gamma_{\phi_j},$$

in which $\partial_T^2 \Gamma_{\phi_1} = g \partial_T \bar{n}_a$ and $\partial_T \Gamma_{\phi_2} = 2g[(1 + \tilde{\mathcal{K}}) \partial_T \bar{n}_a + \bar{n}_a \partial_T \tilde{\mathcal{K}}]$.

Thus, the memory efficiency Eq. (D4) is expressed as

$$\begin{aligned} \mathcal{A} &\simeq \frac{[(1 + \tilde{\mathcal{K}}) \partial_T \bar{n}_a + \bar{n}_a \partial_T \tilde{\mathcal{K}}]^2}{(1 + \tilde{\mathcal{K}}) \partial_T^2 \bar{n}_a} \\ &= (1 + \tilde{\mathcal{K}}) \left[1 + \frac{\partial_T \tilde{\mathcal{K}} / (1 + \tilde{\mathcal{K}})}{\partial_T \bar{n}_a / \bar{n}_a} \right]^2 \end{aligned}$$

We introduce two dimensionless temperature responsivities:

$$S_{\bar{n}_a} = \partial_T \bar{n}_a / \bar{n}_a, \quad S_{\tilde{\mathcal{K}}} = \partial_T \tilde{\mathcal{K}} / (1 + \tilde{\mathcal{K}}),$$

and obtain the compact factorized form

$$\mathcal{A} \simeq (1 + \tilde{\mathcal{K}}) \left(1 + \frac{S_{\tilde{\mathcal{K}}}}{S_{\bar{n}_a}} \right)^2. \quad (\text{D5})$$

Equation (D5) makes the physics transparent: The prefactor $(1 + \tilde{\mathcal{K}}) \geq 1$ is a pure amplitude gain from correlations. It quantifies how much the correlated absorber fluctuations increase the total phase variance seen by the probe relative to the independent-tooth baseline. The squared factor $(1 + S_{\tilde{\mathcal{K}}}/S_{\bar{n}_a})^2$ encodes a responsivity competition between the population slope $S_{\bar{n}_a}$ and the kernel slope $S_{\tilde{\mathcal{K}}}$. When $S_{\tilde{\mathcal{K}}}$ has the same sign as $S_{\bar{n}_a}$, correlations sharpen the temperature dependence of the dephasing and the QFI is further enhanced. When $S_{\tilde{\mathcal{K}}}$ has the opposite sign, the kernel partially cancels the population responsivity and correlations can suppress the QFI below the memoryless reference ($\mathcal{A} < 1$).

In the Lorentzian kernel model used in Fig. 2, short delays $\Delta \ll \tau_c(T)$ exhibit $\tilde{\mathcal{K}} \approx 1$ and a favorable ratio $S_{\tilde{\mathcal{K}}}/S_n$, so that both factors in Eq. (D5) contribute to an enhancement $\mathcal{A} > 1$. Around the correlation-time contour $\Delta \simeq \tau_c(T)$, the kernel becomes strongly temperature-sensitive, and the sign and magnitude of $S_{\tilde{\mathcal{K}}}/S_n$ drive the competition factor below unity. This produces the observed memory disadvantage $\mathcal{A} < 1$ even though the overall dephasing amplitude is larger than in the memoryless case.

Although we illustrate this behavior using a Lorentzian memory kernel $\mathcal{K}(T, \Delta)$, the structure of Eq. (D5) is generic: for any correlated noise source whose dephasing can be decomposed into a diagonal (hard population)

term and a two-time kernel, the same competition between population responsivity $\partial_T \bar{n}_a / \bar{n}_a$ and correlation responsivity $\partial_T \tilde{\mathcal{K}} / (1 + \tilde{\mathcal{K}})$ will govern whether correlations enhance or suppress metrological performance.

Appendix E: Noise Spectrum Reconstruction

Fig. 3 illustrates how different temporal correlation models for the absorber noise imprint distinct delay dependence in the two-tooth coherence and how the same data can be used to reconstruct the underlying noise spectrum $S_{nn}(\omega)$.

We work in dimensionless units and focus purely on the shape of the decay; all pre-factors are absorbed into a single variance scale. We write the single-tooth and correlation contributions as

$$A_b = \lambda^2 (\tau_1^2 + \tau_2^2) \text{Var}(n_a), \quad A_c = 2\lambda^2 \tau_1 \tau_2 \text{Var}(n_a),$$

and Eq. (A8) becomes

$$C_2(\Delta) = \exp[-A_b - A_c \tilde{\mathcal{K}}(\Delta)]. \quad (\text{E1})$$

In the numerics we intentionally set $\lambda = 0.5$, $\tau_1 = \tau_2 = 3\tau_0$, and $\text{Var}(n_a) = 1$ to maximize the contrast. We sample the delay on a logarithmic grid spanning many decades $10^{-3} \leq \Delta/\tau_0 \leq 10^4$, so that both very short- and very long-delay behavior are resolved.

We consider three representative forms of the normalized kernel $\mathcal{K}(\Delta)$ at a fixed temperature:

a. White-noise-like (quasi- δ -correlated) kernel: Very short correlation time modeled by a narrow Gaussian,

$$\tilde{\mathcal{K}}_{\text{white}} \propto e^{-(\Delta/\sigma_w)^2}, \quad \sigma_w = 10^{-3},$$

normalized so that $\mathcal{K}_{\text{white}}(0) = 1$.

b. Lorentzian-correlated kernel: Exponential decay with correlation time τ_c ,

$$\tilde{\mathcal{K}}_{\text{Lor}} = e^{-\Delta/\tau_c}, \quad \tau_c = 10,$$

again normalized so that $\mathcal{K}_{\text{Lor}}(0) = 1$.

c. 1/f-like, heavy-tailed kernel: Slow, algebraic decay designed to produce a broad low-frequency tail,

$$\mathcal{K}_{1/f} = \frac{1}{1 + (\Delta/\tau_f)^\gamma}, \quad \tau_f = 0.1, \quad 0 < \gamma < 1,$$

with $\gamma = 0.6$ in Fig. 3. This form decays more slowly than exponential and therefore mimics a 1/f-like spectrum over an intermediate frequency range.

For each kernel we compute the corresponding two-tooth coherence Eq. (E1), and normalize by the asymptotic long-delay value

$$C_{2,\infty}^{(j)} = \lim_{\Delta \rightarrow \infty} C_2^{(j)}(\Delta), \quad j \in \{\text{white, Lor, 1/f}\}$$

which removes the delay-independent single-tooth factor. The plotted visibility is therefore

$$\tilde{C}_2^{(j)}(\Delta) = e^{-A_c \tilde{\mathcal{K}}_j(\Delta)},$$

so that all curves start from unity at $\Delta = 0$ and decay toward one as the correlation term switches off.

For reconstruction, we invert the coherence–kernel relation:

$$\tilde{\mathcal{K}}_j^{(\text{rec})}(\Delta) = \frac{-\ln \tilde{C}_2^{(j)}(\Delta) - A_b}{A_c},$$

which coincides with the true $\mathcal{K}_j(\Delta)$ up to small numerical errors. We then compute an estimate of the noise spectrum via a discrete cosine transform,

$$S_{nn}^{(\text{rec})}(\omega) \propto \int_0^\infty d\Delta \tilde{\mathcal{K}}_j^{(\text{rec})}(\Delta) \cos(\omega\Delta),$$

which is implemented numerically as

$$S_{nn}^{(\text{rec})}(\omega_i) = 2 \int_0^{\Delta_{\text{max}}} d\Delta \tilde{\mathcal{K}}_j^{(\text{rec})}(\Delta) \cos(\omega_i\Delta),$$

for a logarithmic grid of frequencies $10^{-4} \leq \omega/2\pi \leq 10^2$. The reconstructed spectra are rescaled so that their maxima are normalized to unity.

We compare three representative models of absorber noise and demonstrate how the corresponding two-tooth coherence encodes their spectral structure.

Panel(a) shows normalized two-tooth coherence $\tilde{C}_2(\Delta)$ (visibility) versus delay Δ on a logarithmic axis for three kernel models: quasi-white noise (narrow, rapidly decaying kernel), Lorentzian-correlated noise (exponential kernel), and a $1/f$ -like heavy-tailed kernel. All traces are normalized such that $\tilde{C}_2(0) = 1$ and share the same single-tooth baseline. The white-noise curve drops rapidly and saturates, reflecting an extremely short correlation time. The Lorentzian curve decays more gradually, while the $1/f$ -like curve displays the slowest, almost power-law-like decay, signaling long-lived correlations extending over many decades in Δ .

Panel(b) shows reconstructed spectra $S_{nn}^{(\text{rec})}(\omega)$ obtained by inverting the coherence to recover $\tilde{\mathcal{K}}(\Delta)$ and applying a cosine transform. Each curve is normalized to its own maximum. The reconstructed white-noise spectrum is nearly flat over a broad intermediate band, with a high-frequency roll-off set by the finite time resolution and a low-frequency roll-off set by the finite maximum delay. The Lorentzian kernel yields a reconstructed spectrum that is peaked at low frequency and decays approximately as $1/(1 + \omega^2 \tau_c^2)$. The $1/f$ -like kernel produces a spectrum that approximates a $1/\omega$ dependence across several decades, again with cutoffs at the extremal frequencies imposed by the finite Δ -window and sampling. Together, these curves demonstrate that the two-tooth visibility encodes enough information to distinguish qualitatively different temporal noise structures via simple Fourier inversion.

Appendix F: Impact of Intrinsic Probe Coherence

In practice, even a long-lived probe has a finite dephasing time T_φ^p , which will impact the probe’s coherence envelopes and therefore their correlation. Here, we include intrinsic probe dephasing and clarify its impact on (i) the QFI of the two-tooth protocol and (ii) the reconstruction of correlated noise spectra.

Memory kernel. The absorber number fluctuations are modeled as a stationary Gaussian process with auto-correlation

$$\mathcal{K}(\tau; T) = \langle \delta \hat{n}_a(t + \tau) \delta \hat{n}_a(t) \rangle_T,$$

which depends on the absorber dynamics and temperature T but not on the probe. In the two-tooth comb, the cross-Kerr interaction couples the probe phase to $\delta \hat{n}_a(t)$ only during the two interaction windows with $\tau_{1,2} \ll T_\varphi^p$. Therefore, the absorber memory kernel $\mathcal{K}(\Delta; T)$ itself is unchanged by any additional probe dephasing process.

Single-tooth coherence envelope. The intrinsic coherence envelope of the probe is taken to be

$$C_p(\tau) = e^{-\Gamma_\varphi^p \tau}, \quad T_\varphi^p = 1/\Gamma_\varphi^p,$$

with a temperature-independent dephasing rate Γ_φ^p . Including intrinsic probe dephasing during the same interaction window τ_1 , Eq. (A4) becomes

$$C_1^{\text{full}}(\tau_1) = C_p(\tau_1) \exp[-(\lambda \tau_1)^2 \bar{n}_a].$$

In practice, single-tooth visibilities are essentially unaffected since $\tau_1 \ll T_\varphi^p$ and hence $C_p(\tau_1) \approx 1$; after delay Δ , it becomes $C_p(\Delta) C_1^{(1)}[-(\lambda \tau_1)^2 \bar{n}_a]$

Two-tooth coherence. We now consider the interval window Δ between the two teeth to be non-negligible compared to T_φ^p , so that intrinsic probe dephasing during this idle period cannot be ignored. The probe coherence just before the second interaction is reduced by a factor $C_p(\Delta)$, while dephasing during each short interaction window remains negligible ($\tau_{1,2} \ll T_\varphi^p$). As a result, the full two-tooth coherence envelope becomes

$$\begin{aligned} C_2^{\text{full}}(\Delta) &= C_p^2(\Delta) C_1^1(\tau_1) C_1^{(2)}(\tau_2) \exp[-2\lambda^2 \tau_1 \tau_2 \mathcal{K}(\Delta)] \\ &= C_p^2(\Delta) C_2(\Delta), \end{aligned} \quad (\text{F1})$$

where $C_2(\Delta)$ is the coherence envelope without probe dephasing, as derived in Eq. (A8). Thus, intrinsic probe dephasing simply attenuates the overall two-tooth visibility as a function of Δ .

Minimal impact on QFI. Substituting the full two-tooth coherence envelope Eq. (F1) into Eq. (B1), we obtain

$$\mathcal{F}_2^{\text{full}}(\Delta) = \frac{e^{-4\Gamma_\varphi^p \Delta} \partial_T^2 C_2(\Delta)}{1 - e^{-4\Gamma_\varphi^p \Delta} |C_2(\Delta)|^2}. \quad (\text{F2})$$

The temperature derivative in the numerator of Eq. (F2), which encodes the memory kernel via $\partial_T \mathcal{K}_a(\Delta; T)$, is unchanged by intrinsic probe dephasing. Only the denominator is modified through the reduced visibility $|C_p(\Delta)|^2$.

In the thermometric regime of interest, all relevant time scales satisfy $\tau_{1,2}, \Delta \ll T_\varphi^p$. In this short-time limit we have

$$\mathcal{F}_2^{\text{full}}(\Delta; T) \simeq \mathcal{F}_2(\Delta; T) + \mathcal{O}(\Gamma_\varphi^p \Delta),$$

in which $\mathcal{F}_2(\Delta; T)$ is expressed as Eq. (B3). Therefore, intrinsic probe dephasing has only a minimal impact on the QFI and the memory efficiency in the operating regime of the protocol.

Noise spectra. To probe low-frequency features of the absorber spectrum $S_{nn}(\omega; T)$, very long delays Δ are required and can become comparable to T_φ^p . Using the full coherence envelope Eq. (F1), and *naively* inverting the visibility with Eq. (C1) (i.e., ignoring intrinsic probe dephasing) yields an *effective* autocorrelation

$$\begin{aligned} \mathcal{K}_m &= -\frac{1}{2\lambda^2\tau_1\tau_2} \left[\lambda^2(\tau_1^2 + \tau_2^2) \bar{n}_a + \ln C_2^{\text{full}}(\Delta) \right] \\ &= \mathcal{K}_a(\Delta) + \frac{2\Gamma_\varphi^p}{2\lambda^2\tau_1\tau_2} \Delta, \end{aligned} \quad (\text{F3})$$

where $\mathcal{K}_a(\Delta)$ is the true absorber autocorrelation function in the absence of probe dephasing. Intrinsic probe dephasing thus appears as a known linear-in- Δ bias in the reconstructed kernel if it is not explicitly accounted for.

Equivalently, in the frequency domain the factor $C_p(\Delta)$ acts as a known apodization of the delay-domain data and imposes an effective infrared cutoff at $\omega_{\min} \sim 1/T_\varphi^p$ in the reconstructed spectrum.

For accurate correlated-noise spectroscopy at long delays, the probe envelope therefore needs to be calibrated. A straightforward procedure is to measure the probe coherence envelope $C_p(\Delta)$ independently with the thermal absorber decoupled, then divide the experimental two-tooth visibility by $C_p(\Delta)$ to obtain the ideal visibility $C_2(\Delta)$ of Eq. (A4). The corrected coherence can then be used in Eq. (C1) and Eq. (C2) to reconstruct $\mathcal{K}_a(\Delta)$ and $S_{nn}(\omega)$ without bias from intrinsic probe dephasing.